FIRST-PRINCIPLES MOLECULAR DYNAMICS STUDY OF THE STRUCTURE AND TRANSPORT PROPERTIES OF LiF-NaF WITH UF_4 AND ThF_4

BY

VITOR FERREIRA GRIZZI

THESIS

Submitted in partial fulfillment of the requirements
for the degree of Master of Science in Nuclear, Plasma, and Radiological Engineering
in the Graduate College of the
University of Illinois Urbana-Champaign, 2023

Urbana, Illinois

Master's Committee:

Professor Yang Zhang (YZ), Advisor
Professor Brent J Heuser

Abstract

A thorough understanding and characterization of the thermophysical and transport properties of molten salts are essential for the efficient operation, optimized design, and safety management of Molten Salt Reactors (MSR). However, experimental investigations of molten salts for nuclear applications can be challenging due to factors such as high temperatures, corrosion, purity and composition control, as well as health and safety concerns. As an alternate approach, first-principles molecular dynamics simulations were employed to calculate the thermophysical and structural properties of eutectic LiF-NaF mixed with either UF_4 or ThF_4. The simulations reveal that the addition of uranium or thorium results in a pre-peak in the structure factor, which suggests intermediate-range ordering. The implications of this structural rearrangement on the salt's properties are analyzed. This study emphasizes the connection between the salt's structure and its properties, highlighting how the incorporation of nuclear fuel can influence the properties of the salt in an unexpected manner.

To my family and friends.

Acknowledgments

This project would not be possible without the support of the whole NPRE department and my advisor professor YZ. I am also grateful to my colleagues from YZ's research group for their guidance and insightful discussions. Furthermore, I would like to acknowledge Kirk Sorensen and Kurt Harris at Flibe Energy for the suggestion to study LiF-NaF. Finally, I would like to say thank you to my family and friends for all the love and support.

Table of contents

List of Abbreviations

MSR	Molten Salt Reactor
MD	Molecular Dynamics.
AIMD	Ab-Initio Molecular Dynamics.
FPMD	First-Principles Molecular Dynamics.
DFT	Density Functional Theory.
NVT	Canonical Ensemble.
NpT	Isothermal-isobaric Ensemble.
NVE	Microcanonical Ensemble.
SCF	Self-Consistent Field.

List of Symbols

τ	Relaxation Time.
τ_0	Residence Time.
ρ	Density.
α_v	Volumetric Thermal Expansion Coefficient.
η	Shear Viscosity.
c_p	Specific heat capacity at constant pressure.
c_v	Specific heat capacity at constant volume.
$\sigma^{\alpha\beta}$	Stress tensor component along cartesian coordinates α and β.

Chapter 1

Molten Salt Reactors

The quest to develop advanced nuclear systems like Molten Salt Reactors (MSRs) stems from the necessity to address global warming while ensuring both energy sustainability and reliability. In this chapter, the history and potential benefits of MSRs are dicussed.

1.1 History

The study of molten salt reactors dates back to the late 1940's. The initial motivation behind this research was to develop a nuclear-powered airplane [1]. The first MSR was developed in Oak Ridge National Laboratory (ORNL) in the early 1950's to study the nuclear stability of the circulating fuel system. It used a ternary fluoride salt composed of NaF, ZrF_4, and UF_4. Even though the concept of a nuclear-powered airplane was eventually abandoned, the research findings from this program played a crucial role in the development of MSRs for electricity generation as we know them today.

In the early 1960's ORNL and the U.S. Atomic Energy Commission (AEC) acknowledged the potential of MSRs and the Molten-Salt Reactor Experiment was devised. It used LiF-BeF_2-ZrF_4-UF_4 as primary coolant, LiF-BeF_2 as secondary coolant, and graphite as moderator. One of the key discoveries during this experiment was the fact that LiF and BeF_2 could be separated from rare earth elements by vacuum distillation at temperatures around 1000 °C [1], [2].

In the early 1970s the funding from the AEC to develop molten salt reactors was abruptly terminated due to corrosion issues observed during experiments [3]. Despite limited funding, Oak Ridge National Laboratory (ORNL) continued its molten salt reactor research program on a smaller scale until the early 1980s. It was not until the beginning of the 21st century that the interest in MSRs resurged due to the selection of MSRs as one of the six Generation IV advanced nuclear reactor designs. In the present time, MSRs is an active area of research and it is hailed as one of the most promising Generation IV designs [4]–[7], with multiple startups undertaking the quest of developing reliable and efficient MSRs.

1.2 Overview

There are two main reactor designs that use molten salts. The first uses a standard solid fuel and the molten salt acts as coolant. In the second the molten salt serves both as coolant and fuel, and the term MSR is often used to specifically refer to this second reactor design. MSRs feature a unique design in which the fuel, typically ThF_4 or UF_4, is directly dissolved in the molten salt. In a conventional MSR, there are two circuits moving around the molten salt. The primary loop contains the salt with dissolved fuel. The molten salt in the primary loop of a molten salt reactor circulates through the reactor core, serving simultaneously as the coolant and the fuel. The secondary loop, on the other hand, contains pure molten salt with no dissolved fuel. The molten salt in the primary loop of a molten salt reactor transfers thermal energy to the molten salt in the secondary loop. This secondary loop then flows through another heat exchanger to generate steam, which drives a turbine. It's worth noting that the molten salts in the two loops can be different. In most designs carbon is used as moderator.

There are several advantages associated with MSR. One of the main advantages is online fuel processing. Because the fuel is dissolved in the coolant, it can be processed during operations to remove undesired fission products that compete with fissile and/or fertile materials for neutrons, which translates into a very high fuel efficiency. Additionally, unlike traditional reactors, there is no need to shut down the reactor for refueling as it can be refueled continuously. Since the fuel is dissolved in the salt, there is also no need to fabricate fuel pellets. This avoids engaging in rigorous and complex manufacturing processes, decreasing the overall operation complexity and saving money [5]. On top of that, no cladding, fuel duct, nor grid spacers are necessary. This simplified design decreases the neutron loss in the structure and increases efficiency.

Regarding safety there are also several benefits unique to MSRs. Due to the high boiling point of the salt, the reactor can operate at very high temperatures while maintaining pressures near or at atmospheric levels. This feature reduces the need for thick, robust containment vessels, thereby simplifying the reactor's design, and decreasing maintenance and capital costs. This is a substantial improvement over the currently dominant light water reactors (LWR) which operate at pressures ranging from approximately 70 to 160 atmospheres and require sturdy containment vessels. Another safety perk of MSRs is the chemical inertness of the salt with water and air [8], which eliminates the risk of hydrogen explosions. MSRs also have inherent safety mechanisms, such as negative temperature and void coefficients [9]. Furthermore, in case of an unexpected even where the temperature in the reactor rises excessively, a freeze valve designed to melt at high temperature come into play. When the valve melts, the salt in the core is drained to a heat-sink tank that is filled with neutron poison. This setup rapidly cools the salt and reduces the fission rate [10].

There are, however, some disadvantages and challenges related to MSR. One of the main challenges is corrosion. Molten salts can be highly corrosive, particularly at the high temperatures of operation [11]. Impurities seem to play a major role in the corrosion process [12], mainly oxygen and water dissolved in the salt. Another problem is the mobile fission products. Since the fuel is dissolved within the circulating molten salt, the fission products also circulate in the reactor and interact with the surrounding structure. Therefore, most of the material inside the reactor becomes radioactive, complicating maintenance, material handling, and eventual decommissioning. Also, in case of a power outage, heaters are necessary to keep the salt in the liquid state.

1.3 Molten Salt Screening

Because the molten salt plays so many roles in a MSR, a thorough understand of its physical properties is necessary. Thermophysical properties, such as thermal conductivity, specific heat capacity, and thermal expansion, dictate how effectively the reactor can transfer and dissipate heat. This directly affects the reactor's operational stability and efficiency. Failing in accurately determine these properties can lead to inefficient reactor designs and even safety risks due thermal stresses. Other properties, such as viscosity, are crucial for performing simulations and understanding the flow of the molten salt in the reactor.

Out of all molten salt candidates, fluoride salts are particularly appealing due to their low vapor pressure, high solubility of uranium, good heat transfer properties, stability under irradiation, and neutron moderator capabilities [1], [13]. Using variants of fluoride salts with a lower melting point is advantageous because it reduces the risk of the molten salt solidifying and makes the reactor start-up simpler. Chloride salts are also a popular option, sharing many of the benefits of fluoride salts due to the chemical similarities between fluorine and chlorine.

Experimentally characterizing the properties of molten salts poses several challenges. The high temperatures of interest of approximately 750 °C, and the inherent corrosiveness of the salt require specially designed experimental settings and equipment. There are also concerns regarding the salt's purity. Contaminants can emerge either from interactions between the salt and its container or be initially present in the salt, and even small amounts of these contaminants can impact the measured properties. Given these challenges, conducting an initial computational screening of candidate molten salts is essential to save time, resources, and avoide the aforementioned problems.

Chapter 2

Molecular Dynamics

Molecular Dynamics (MD) is a computer simulation tool used to evolve a system of atoms and/or molecules over time to study their interactions and compute the system's properties. The system evolves in time according to some prescribed interatomic potential in case of classical MD or according to a Hamiltonian in case of AIMD.

Frequently, the goal of MD simulations is to compute the system's equilibrium properties, such as density, bulk modulus, specific heat, viscosity, and thermal conductivity. According to statistical mechanics, calculating these equilibrium properties analytically requires averaging them across the entire phase space, which involves solving the following integral

$$\langle A(\{\mathbf{r}_i, \mathbf{p}_i\})\rangle = \int_{-\infty}^{\infty} ... \int_{-\infty}^{\infty} A(\{\mathbf{r}_i, \mathbf{p}_i\})\, \rho(\{\mathbf{r}_i, \mathbf{p}_i\})\; d\mathbf{r}_1 \,...\, d\mathbf{r}_N \, d\mathbf{p}_1 \,...\, d\mathbf{p}_N \tag{2.1}$$

where $\{\mathbf{r}_i, \mathbf{p}_i\}$ denotes the set of all atomic coordinates and momenta in the system $\{\mathbf{r}_1, ..., \mathbf{r}_N, \mathbf{p}_1, ..., \mathbf{p}_N\}$, and $\rho(\{\mathbf{r}_i, \mathbf{p}_i\})$ is the phase space probability density or distribution function. However, solving this integral is a daunting task because of two main reasons. The first reason is that it is a $6N$-dimensional integral, where

N is the number of atoms in the system. The second reason is that in order to find the phase space distribution function $\rho(\{\mathbf{r}_i, \mathbf{p}_i\})$, it is necessary to compute the partition function of the system, which is virtually impossible for most systems of interest. A workaround is to completely ignore the full partition function and calculate the desired equilibrium property using only a set of points sampled from the equilibrium phase space respecting the system's macrostate. The real equilibrium property $\langle A(\{\mathbf{r}_i, \mathbf{p}_i\})\rangle$ is then approximated as a simple average over these sampled points and this is the essence of MD. Simply put, MD samples the relevant portion of the system's phase space given a macrostate acting as constraint, thereby avoiding the use of Equation 2.1. The term "constraint" means that only certain regions of the phase space have a non-zero probability density and thus can be sampled during the simulation. In other words, only the points in phase space consistent with the macrostate are sampled.

A macrostate is a set of thermodynamic properties that define the system's state. By maintaining certain properties constant, a specific thermodynamic ensemble is defined. The most common ensembles are the microcanonical (NVE), canonical (NVT), and isothermal-isobaric (NpT). These ensembles differ by the quantities they keep fixed, where N stands for number of atoms, V for volume, E for energy, P for pressure, and T for temperature. The functional form of the partition function is also different for each ensemble. For instance, in the microcanonical ensemble each microstate (i.e. each point in phase space) consistent with the macrostate has the same probability density, whereas in the canonical ensemble the probability of a microstate is Boltzmann-weighted according to the energy of that microstate.

The idea of approximating an ensemble average with a time average stems from the ergodic hypothesis in statistical mechanics. The ergodic hypothesis is a fundamental concept in statistical mechanics that allows for the substitution of ensemble averages for time averages and vice-versa. According to the ergodic hypothesis, given enough time the system will visit all of its accessible microstates in phase space according to the distribution function $\rho(\{\mathbf{r}_i, \mathbf{p}_i\})$. Therefore, for an ergodic system, the long-time average of a system's property will be equal to its ensemble average.

2.1 Classical Molecular Dynamics

In classical MD, an interatomic potential $V(\{\mathbf{r}_i\})$ is defined and the atoms interact over the course of the simulation according to the provided interatomic potential. The atoms are treated as hard spheres and the electronic structure is completely ignored. Interatomic potentials consist of a fixed functional form whose parameters are fitted from experiments or quantum mechanical calculations. With the potential $V(\{\mathbf{r}_i\})$ in hands, the total force acting on atom j can be easily calculated using

$$\mathbf{F}_j = -\nabla_{\mathbf{r}_j} V(\{\mathbf{r}_i\}) \tag{2.2}$$

Since the potential is described by a closed analytical expression, the resulting force is also a closed analytical expression. The typical procedure in a MD simulation involves initializing the positions and velocities of particles, calculating the forces acting on each atom using Equation 2.2, numerically integrating Newton's equations of motion $\mathbf{F} = m/a$ over a time step dt, and then updating the positions and velocities of all particles. After updating the atomic positions and velocities, a new phase space point is sampled. This entire process is repeated until the predetermined number of time steps set by the user is reached. From this description, it is intuitive to understand MD as essentially a technique for discretely exploring or sampling the phase space. Thus, a MD simulation can be viewed as a trajectory or curve in the phase space.

2.2 Ab-Initio Molecular Dynamics

The second flavor of MD is ab-initio or first-principles molecular dynamics. Here, the forces are calculated from first principles using quantum mechanics. To do so, the many-body Schrödinger equation must be solved. This means finding the many-body wave function $\psi(\{\mathbf{R}_i, \mathbf{r}_i\})$ where $\mathbf{R}_i$ refers to the coordinates of the nuclei and $\mathbf{r}_i$ to the coordinates of the electrons. The full Hamiltonian is of the form

$$\hat{H} = \hat{T}_n + \hat{T}_e + \hat{V}_{n-e} + \hat{V}_{n-n} + \hat{V}_{e-e} \tag{2.3}$$

where the first term on the right-handed sided is the kinetic energy of the nuclei, the second term is the kinetic energy of the electrons, the third term is the nucleus-electron interaction, the fourth term is the nucleus-nucleus interaction, and the fifth term is the electron-electron interaction. Expanding each term of the Hamiltonian operator yields

$$\begin{aligned} \hat{H}(\{\mathbf{r}_i\}, \{\mathbf{R}_i\}) = &- \sum_i \frac{\hbar^2}{2M_i} \nabla^2_{\mathbf{R}_i} - \sum_i \frac{\hbar^2}{2m_e} \nabla^2_{\mathbf{r}_i} - \sum_i \sum_j \frac{Z_i e^2}{|\mathbf{R}_i - \mathbf{r}_j|} \\ &+ \sum_i \sum_{j>i} \frac{Z_i Z_j e^2}{|\mathbf{R}_i - \mathbf{R}_j|} + \sum_i \sum_{j>i} \frac{e^2}{|\mathbf{r}_i - \mathbf{r}_j|} \end{aligned} \tag{2.4}$$

where e is the elementary charge, M the mass of the nucleus, m_e the mass of the electron, Z the atomic number of the nucleus, and the factor of $\frac{1}{4\pi\epsilon_0}$ of the last three terms on the right-handed side was set to 1 for conciseness. An analytical solution to the many-body Schrodinger equation under the Hamiltonian described in Equation 2.4 is impossible, and using traditional grid-based numerical methods is unfeasible due to the very high dimensionality of the equation. Thus, we first need to make some approximations. One of the main approximations used in AIMD is the Born-Oppenheimer (BO) approximation. The idea is that the wave function of the electrons can be decoupled from the wave function of the nuclei, or mathematically

$$\psi(\{\mathbf{r}_i\}, \{\mathbf{R}_i\}) = \psi(\{\mathbf{R}_i\})\ \psi(\{\mathbf{r}_i\}; \{\mathbf{R}_i\}) \tag{2.5}$$

where $\psi(\{\mathbf{R}_i\})$ refers to the nuclei wave function and $\psi(\{\mathbf{r}_i\}; \{\mathbf{R}_i\})$ represents the electronic wave function given a fixed nuclei configuration or geometry. Under this approximation, the electronic wave function depends parametrically on the nuclei coordinates $\{\mathbf{R}_i\}$. Intuitively, the BO approximation is grounded on the fact that the time-scale of electron motion is much faster than the nuclear motion. It assumes that the wave function of the electrons instantaneously respond to a change in the nuclei configuration (adiabatic assumption), and the nuclei move only in the potential energy surface of the electronic ground state (there is no excited-state dynamics). However, when these assumptions are not valid and the electronic motion is coupled to nuclear motion, the BO approximation fails. In such cases, non-adiabatic molecular dynamics has to be used [14].

By employing the BO approximation, the next step is to solve the Schrödinger equation for the electrons, and find the electronic wave function $\psi(\{\mathbf{r}_i\}; \{\mathbf{R}_i\})$ and eigenvalues $\varepsilon(\{\mathbf{R}_i\})$, both depending parametrically on the nuclei coordinates. Because the nuclei coordinates are fixed, the kinetic energy term $\hat{T}_n$ in Equation 2.3 goes to zero, the nuclei-nuclei interaction $\hat{V}_{n-n}$ becomes a constant, and the nuclei-electron interaction term $\hat{V}_{n-e}$ simplifies since now it represents the energy of the electrons under a static positive charge distribution or background. Note that now $\hat{V}_{n-e}$ can be effectively viewed as an external potential acting on the many-electron system. However, even under this simplified Hamiltonian it is still impossible to exactly solve the Schrödinger equation because it remains very complicated, mostly due to the electron-electron interaction term V_{e-e}.

There are several different methods to approximate the solution of the Schrödinger equation for a many-electron system. These approaches range from the simple Hartree-Fock method, to more complex post-Hartree-Fock methods such as Coupled Cluster[15] and Møller-Plesset Perturbation theory [16]. However, the most popular one used in AIMD packages is Density Functional Theory (DFT), which is based in the Hohenberg-Kohn (HK) theorems [17]. The first HK theorem proves that the ground state properties of a many-electron system are functionals of the system's electron density $n(\mathbf{r})$, and therefore $n(\mathbf{r})$ uniquely determines all ground state properties of a many-electron system including the many-body wave function. This means that finding the electron density is equivalent to finding all equilibrium properties of interest. By focusing on the electron density which is a function of only three spatial coordinates, the many-electron problem is reduced from dealing with $3N$ variables to just three spatial variables, where N is the total number of electrons in the system. This simplification is one of the cornerstones of DFT's computational efficiency. The second HK theorem shows that the true electron density minimizes an energy functional of the form

$$E[n(\mathbf{r})] = T[n(\mathbf{r})] + V_{ext}[n(\mathbf{r})] + E_{Hartree}[n(\mathbf{r})] + E_{xc}[n(\mathbf{r})]. \tag{2.6}$$

where $T[n(\mathbf{r})]$ is the kinetic energy of the many-electron system, $V_{ext}[n(\mathbf{r})]$ is a general external potential that the many-electron system is subjected to, the Hartree energy $E_{Hartree}[n(\mathbf{r})]$ describes the electron-electron Coulombic repulsion, and the exchange-correlation (XC) energy $E_{xc}[n(\mathbf{r})]$ represents the rest of the energy not captured by the kinetic and Hartree terms. Note that while the term external potential is very broad and can potentially encompass any effect that can be modeled as an external potential acting on the many-electron system, it primarily describes the Coulombic interactions between the electrons and the fixed nuclei background.

The main issue with Equation 2.6 is the XC energy term. More specifically, the

XC energy describes exchange interactions that arises from the antisymmetrization requirements of fermionic wave functions (Pauli exclusion principle), and N-body correlations in the electron dynamics. It essentially describes complex interactions not addressed by the other terms in the energy functional. The exact form of the XC energy functional is not known, so approximations must be made. Two of the most common approximations are the local density approximation (LDA) and the generalized gradient approximations (GGA) [18], [19]. Generally speaking, the former considers only the electron density at each point in space, while the latter considers both the electron density and its gradient. More accurate approximations to the XC energy such as the Meta Generalized Gradient Approximation (MetaGGA) also considers the Laplacian of the electron density.

By choosing an approximation for the XC functional, the total energy of the many-electron system can be calculated provided that the electron density $n(\mathbf{r})$ is known. Yet, finding the electron density is not easy and requires solving the Schrödinger equation for the many-electron system which is intractable even under the BO approximation, and here is where DFT comes into play. The electron density of a many-electron system can actually be determined by solving a Schrödinger-like equation, known as the Kohn-Sham (KS) equations [20]. The KS equations describe a fictitious system of non-interacting particles that has the same electron density as the original system of interacting particles. Thus, there is a one-to-one mapping between the electron density of this fictitious system and the real system of interest. The KS equations are given by

$$\left(-\frac{\hbar^2}{2m}\nabla^2 + V_{eff}(\mathbf{r})\right)\varphi_i = \varepsilon_i\varphi_i \tag{2.7}$$

where φ_i and ε_i are, respectively, the i-th Kohn-Sham orbital and energy, and V_{eff} is the effective external potential to which the fictitious system of fermions is subjected.

Note that the XC energy, the Hartree energy, and the external potential in the original system were all lumped into V_{eff}. There are N KS equations to solve, where N is the number of electrons in the original system. Because the KS system is non-interacting, the total KS wave function becomes a single Slater determinant constructed from the ground state KS orbitals φ_i, which considerably facilitates things.

Because the effective potential V_{eff} in which each particle moves depends on the distribution of all the other particles, the KS equations have to be solved in a self-consistent manner. When the KS equations are solved to yield the KS oribtals and energies, the density $n(\mathbf{r})$ that mimics the electron density of the original system is straightforward to calculate through

$$n(\mathbf{r}) = \sum_i |\varphi_i|^2 \tag{2.8}$$

Solving the KS equations is the essence of DFT. Additionally, note that DFT is an exact theory in principle. However, in practical applications, exact calculations cannot be performed because the true form of the exchange-correlation functional is not known. This means that DFT only produces approximate results because the an approximation to the XC functional is used. If the exact XC functional for a system were known, then the results obtained from DFT calculations would also be exact.

By solving the KS equations and finding the electron density of the many-body system, the ground state properties are found, and the forces acting on each atom can be calculated using Hellmann-Feynman's theorem. Therefore, AIMD is the propagation of atoms in time using Hellmann-Feynman forces derived from electronic structure calculations.

Chapter 3

Results and Discussion

3.1 Computational Methods

The AIMD simulations were performed using Vienna *Ab-Initio* Simulation Package (VASP) version 5.4.4 [21], [22]. The simulation cell contained eutectic salt LiF-NaF (3:2 mol%) plus the fuel additive UF_4 and ThF_4. The uranium system consisted of 56 F, 24 Li, 16 Na, and 4 U atoms, while the thorium system consisted of 56 F, 24 Li, 16 Na, and 4 Th atoms. In both cases, the molar concentration of the fuel correspond to 9.1 mol%.

Periodic boundary conditions were used to avoid surface effects since the goal is to calculate bulk properties. Six temperatures were simulated: 973 K, 1073 K, 1173 K, 1273 K, 1373 K, and 1474 K. Perdew-Burke-Ernzerhof (PBE) functional [23] was used as the generalized gradient approximation to the exchange-correlation energy. The projector augmented wave (PAW) method [24] was used to avoid using many Fourier components to describe the rapid oscillations of the valence electrons wave function near the nuclei. The chosen PAW-PBE pseudopotentials were F ($2s^2$ $2p^5$), Li_sv ($1s^2$ $2s^1$), Na_pv ($2p^6 3s^1$), U ($6s^2$ $7s^2$ $6p^6$ $6d^2$ $5f^2$), and Th ($6s^2$ $7s^2 6p^6$ $6d^1$ $5f^1$) where the parenthesis specifies the electrons not included in the pseudopotential and therefore treated explicitly. The energy cutoff for the plane-wave basis set was 600 eV and a Γ-centered 1 × 1 × 1 k-point mesh was used. Sampling only the Γ-point of the Brillouin Zone (BZ) is justified because the simulation box size is large, which means that the BZ is small. DFT-D3 [25] with zero damping was used as a dispersion correction to the self-consistent Kohn-Sham energy. For the simulations that involved uranium atoms, DFT+U method was used to improve the description of its highly correlated d- and f- valence electrons. More specifically, Dudarev *et al.* rotationally invariant approach to DFT+U [26] was used. The U parameter, which sets the effective on-site Coulombic interactions, was taken from Reference [27] and set to 2.0 eV for the uranium atoms.

First, a NpT simulation was performed for all three systems to determine the respective equilibrium simulation cell size. For the NpT runs, Langevin thermostat and the friction coefficient was set to 10 ps^{-1} for all atoms. A 90 ps was performed at each temperature. The first 40 ps were considered pre-equilibration and thus discarded. The last 50 ps were used to find the equilibrium simulation box. Next, a 100 ps simulation in the NVT ensemble was performed with the equilibrium volumes calculated from the NpT runs. Again, the first 40 ps were considered pre-equilibrium and the last 60 ps were used to calculate the properties of the salt.

3.2 Thermophysical and Transport Properties

3.2.1 Density

Density is one of the most important properties because it is presented in virtually all equations that describes the system. In the NpT ensemble, the volume of the simulation box is allowed to fluctuate to maintain the specified pressure fixed. Over the course of the simulation, the average density can be found by dividing the mass

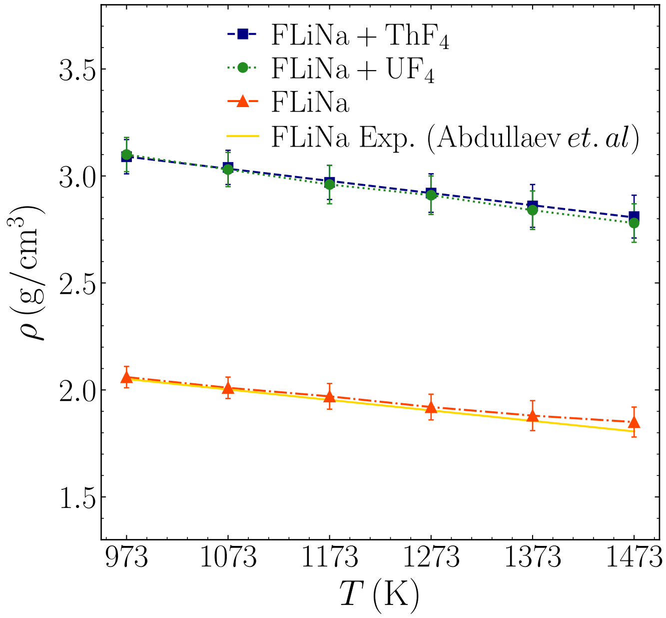

Figure 3.1: Comparison between simulated densities and experimental results.

of the system by the average box volume $\langle V \rangle$.

Figure 3.1 shows the simulated density for the three simulated systems and the experimental results [28] of the pure eutectic system. The error bars are the standard deviation of the density throughout the simulation. For the systems with uranium and thorium comparison was not possible because no experimental data was available. However, for the pure system, there is a very good agreement between simulation results and experimental data. At low temperatures, the simulation error is less than 1%, increasing to 2% at the highest temperature. This close agreement validates the parameters used in the simulation. Figure 3.1 shows that when ThF_4 and UF_4 are added to the pure system, the density increases by roughly 50%. A increase is expected because F, Li, and Na are very light elements while Th and U are one of the heaviest ones.

3.2.2 Thermal Expansion

The volumetric thermal expansion coefficient is a measure of how much the volume of the material changes as temperature increases. It is an important property for MSRs because it appears in the calculation of the temperature coefficient of reactivity. In a MSR, the fuel and moderator are dissolved in the salt. In case of a nuclear accident where the reactor's temperature rises, the expansion of the salt would cause the molar concentrations of both the moderator and the fuel to decrease. The decrease in the moderator concentration hinders the moderator's ability to slow down neutrons, and the decrease in the fuel molar concentration decrease the fission density. Both effects put together results in a negative contribution to the temperature coefficient of reactivity. Therefore, it is desirable to have a salt that expands as the temperature increases. The thermal expansion coefficient can be directly calculated from the density

$$\alpha_v = -\frac{1}{\rho}\frac{\partial \rho}{\partial T}. \tag{3.1}$$

Figure 3.2 depicts the volumetric thermal expansion of all three simulated systems and the experimental results [28]. The experimental thermal expansion coefficient was roughly 20% higher than the simulated one. In classical MD, the thermal expansion depends on the shape of interaction potential. In DFT, it will depend mostly on the choice of exchange-correlation functional. Although the result was relatively close to the experimental value, choosing a different exchange-correlation function, especially one with a stronger non-local character that better capture dispersion effects [29], may improve the agreement. The downside is that such exchange-correlation functionals are more computationally expensive and the calculations are harder to converge. Nevertheless, from the simulation results it seems like adding the fuel has little to no impact on the thermal expansion coefficient of the molten salt.

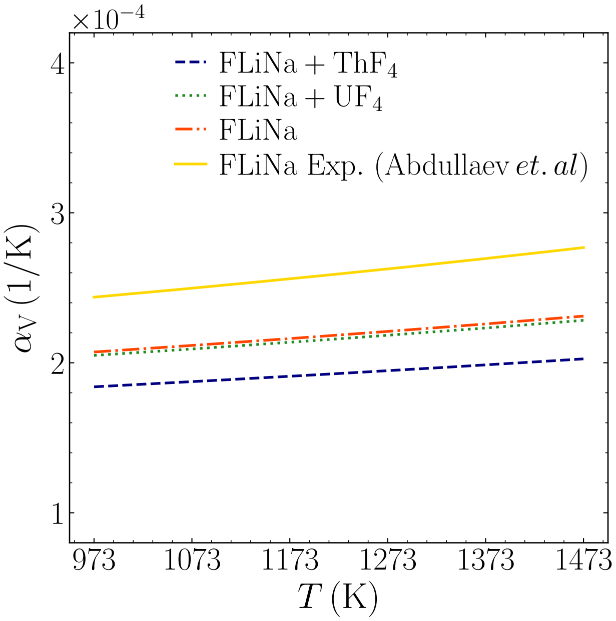

Figure 3.2: Thermal expansion coefficient α_v for the three simulated systems and the experimental result for the pure system [28]. The full line indicates the experimental result whereas the dashed lines depicts the results of the simulation.

3.2.3 Heat Capacity

Heat capacity is one of the most important quantities in the screening of molten salts for energy storage applications because it quantitatively describes the capacity of the salt to store heat. It tells the amount of energy needed to increase the temperature of the system by one degree Kelvin. The heat capacity is closely related to the degrees of freedom of the system. When energy is added into a system, it is partitioned among the terms of the Hamiltonian. This partition depends on how the Hamiltonian depends on the microscopic variables $\mathbf{r}$ (position) and $\mathbf{p}$ (momentum). More degrees of freedom translates into more ways to share the energy that is being added, and therefore more energy is required to elevate the system's temperature.

At low temperatures the heat capacity increases with the temperature because new modes become accessible as temperature rises. However, beyond a certain threshold temperature, all vibrational modes are already unlocked, causing the heat capacity to plateau and remain constant even if the temperature keeps increasing. As a result, the total energy of the system will linearly increases with temperature. This holds true until the system becomes a gas, in which case there is a sharp drop in the heat capacity.

Classically, heat capacity is defined as the derivative of the energy with respect to temperature at a constant pressure

$$C_p = \frac{\partial E}{\partial T}\Big|_P \tag{3.2}$$

or volume

$$C_v = \frac{\partial E}{\partial T}\Big|_V . \tag{3.3}$$

An alternative way to calculate $\mathrm{C_p}$ and $\mathrm{C_v}$ [30][31] in MD simulations is by looking at the the fluctuation of the enthalpy in the NpT ensemble

$$C_p = \frac{\langle H^2 \rangle - \langle H \rangle^2}{k_b T^2} \tag{3.4}$$

or the fluctuation of the total energy in the NVT ensemble

$$C_v = \frac{\langle E^2 \rangle - \langle E \rangle^2}{k_b T^2} \tag{3.5}$$

This is a fundamental result that can be derived by working Equations 3.2 and 3.3 for each ensemble. This method is sometimes employed to calculate the specific heat in MD simulations because the standard deviation of the total energy is straightforward to obtain. However, McGaughey *et al.*[32] recommend using Equations 3.2 and 3.3. Although these two methods in principle should yield the same result, the classic thermodynamic definition often produces more accurate results. For that reason, the specific heat capacity at constant pressure reported here was calculated using Equation 3.2.

Figure 3.3 shows the enthalpy as a function of temperature for each system. As expected at high temperatures, the enthalpy is increasing linearly with the temperature. As a consequence, the heat capacity is a constant at the simulated temperature range as shown in 3.4. Figure 3.4a shows the specific heat capacity and Figure 3.4b shows the molar heat capacity. When uranium and thorium are added into the system, the specific heat capacity decreases a lot. This result was anticipated because with the inclusion of uranium and thorium, the density of the system rises, leading to a reduction in the degrees of freedom per unit mass which in turn results in a lower specific heat capacity. Conversely, when comparing the molar specific heat of the three simulated systems, it is observed that they are approximately the same. The addition of fuel appears to have a minimal impact on the molar specific heat. In fact, Figure 3.2b shows that adding the fuel slightly increases the molar heat capacity.

3.2.4 Viscosity

Viscosity is also an property important for nuclear applications because it plays an important role in equations governing fluid dynamics. Physically, viscosity is related to the transport of momentum between layers of the fluid. In a viscous fluid, this momentum transport is inefficient, and this leads to a “sluggish“ flow. In a MD simulation, viscosity can be calculated through a specific Green-Kubo relations. In its most general flavor, the Green-Kubo relation reads [33]

$$\psi(\omega) = \lim_{\tau' \to \infty} \int_0^{\tau'} exp(-i\omega\tau) \left\langle A(t_0 + \tau) B(t_0) \right\rangle \, d\tau \tag{3.6}$$

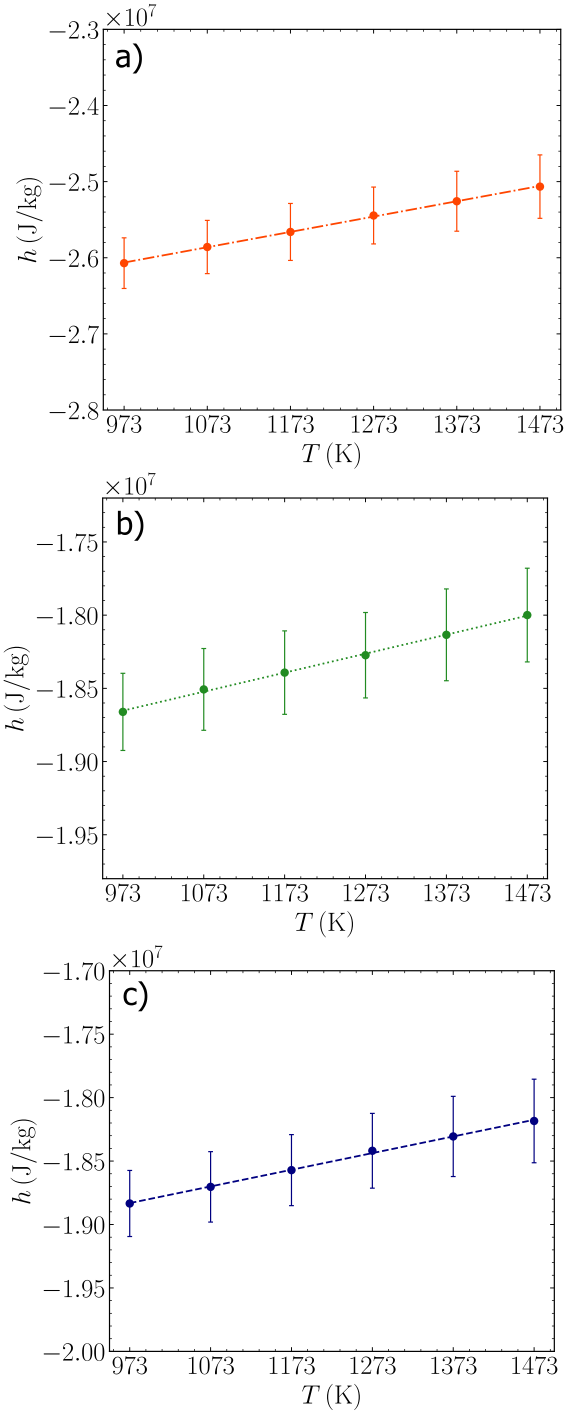

Figure 3.3: Specific enthalpy as a function of temperature for **a)** pure FLiNa, **b)** FLiNa + UF_4, **c)** FLiNa + UF_4.

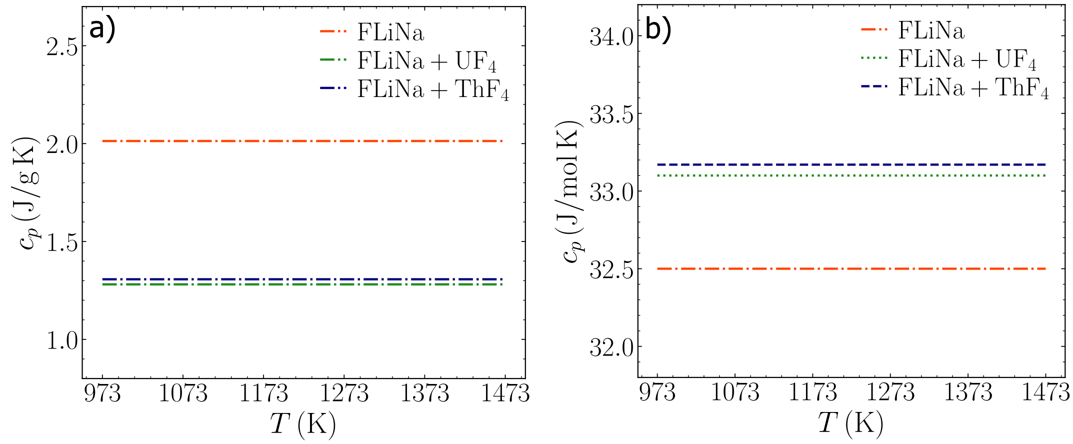

Figure 3.4: **a)** shows the specific heat capacity and **b)** depicts the molar heat capacity for the three different systems.

where $\psi(\omega)$ is a generalized susceptibility, $\langle A(t_0+\tau)B(t_0)\rangle$ is the cross-correlation between two phase space functions $A(\{\mathbf{p}(t),\mathbf{q}(t)\})$ and $B(\{\mathbf{p}(t),\mathbf{q}(t)\})$ where $\{\mathbf{p}(t),\mathbf{q}(t)\}$ denotes the set of $3N$ momenta $\{p_{i\alpha}\}$ and coordinates $\{q_{i\alpha}\}$ of all N atoms in the system at a given time t, and the integral is over the time delay $\tau = t - t_0$ between $A(t)$ and $B(t)$. Intuitively, we can understand $A(t)$ or $B(t)$ as time series describing the realizations of a random variable that represents some property of the system in equilibrium. The Green-Kubo relations are extremely useful in MD simulations because they allow the calculation of transport property from time-correlations of equilibrium properties. It is a very general result that draws from the Fluctuation-Dissipation theorem [34] and describes the collective dissipative response of a system to thermal fluctuations. The transport quantity that is calculated from the Green-Kubo relation depends entirely on the phase space functions $A(\{\mathbf{p}(t),\mathbf{q}(t)\})$ and $B(\{\mathbf{p}(t),\mathbf{q}(t)\})$. A low-frequency limit of Equation 3.6 is often taken, so it simplifies to

$$\psi(\omega) = \lim_{\tau'\to\infty} \int_0^{\tau'} \langle A(t_0+\tau)B(t_0)\rangle \, d\tau \tag{3.7}$$

For viscosity, the Green-Kubo relation becomes

$$\eta = \lim_{\tau' \to \infty} \frac{V}{k_b T} \int_0^{\tau'} \langle \sigma^{\alpha\beta}(t_0 + \tau)\, \sigma^{\alpha\beta}(t_0) \rangle \, d\tau \tag{3.8}$$

where $\langle \sigma^{\alpha\beta}(t_0 + \tau)\, \sigma^{\alpha\beta}(t_0) \rangle$ is the autocorrelation of the three off-diagonal elements of the stress tensor, V the volume of the simulation box, T the temperature of the system and k_b is the Boltzmann constant. Thus, under the Green-Kubo formalism, viscosity is proportional to the amount of correlation of each shear stress component acting on the simulation box with itself. Because liquids are isotropic, the calculation of the viscosity using σ^{xy}, σ^{xz}, or σ^{yz} should yield identical results in the thermodynamic limit. For that reason, the viscosity is determined by considering independent calculations from the three shear components and taking an average.

Figure 3.5 depicts the simulated viscosity for the three systems in an Arrhenius-like plot log(η) vs 1000/T. For pure FLiNa, the viscosity decreases linearly with temperature and is approximately a straight line in the semi-log plot as expected. For the system with uranium, the trend closely resembles a straight line, while for thorium there is a slight deviation from this linear behavior. This is probably due to the high error bars in the simulations involving this two elements. As already discussed, performing AIMD simulations with d- and f-block elements is very challenging due to strong correlation effects of their valence electrons [26],[35]. Convergence of the SCF procedure for these elements is difficult and requires setting additional parameters, increasing the complexity of the simulation. This may explain the larger error bars in the systems containing uranium and thorium compared to the pure system, as well as the deviation from a straight line in the semi-log viscosity plot for the system with thorium.

Overall, adding uranium and thorium has the overall effect to increase the salt's viscosity. For all other thermophysical properties discussed so far, the results for

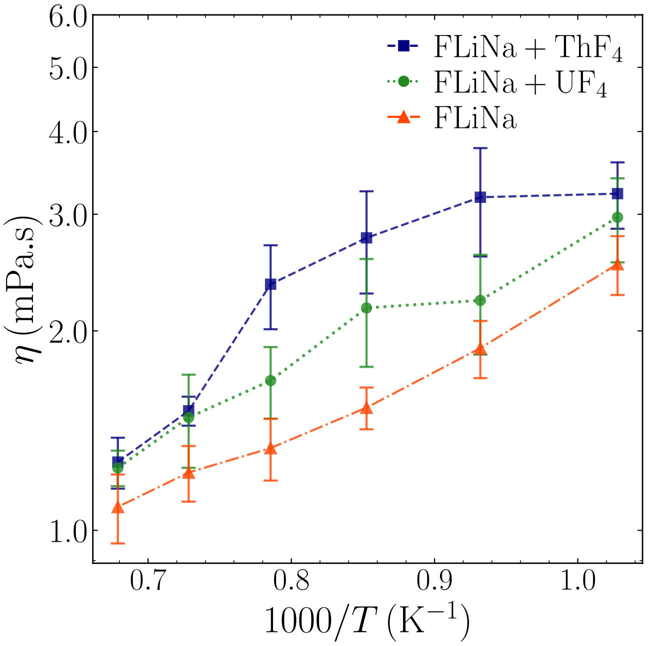

Figure 3.5: Viscosity as a function of temperature calculated of the three simulated systems.

the systems with thorium and uranium were very similar, but for viscosity they seem to differ. While at high temperatures the two viscosities were very close, at the intermediate simulated temperatures the calculated viscosity for the system containing thorium was higher. However, this difference doesn't necessarily mean that the viscosity for the thorium system is in fact greater. The high temperature results are more reliable because the shear stress decorrelation time (here defined as the time delay where the autocorrelation first goes to zero) decreases with increasing temperature. This happens because the system is getting farther from its melting point and thermal effects are becoming more extreme, thereby enhancing phenomena that decorrelate the atom's properties such as collisions. This decrease in the decorrelation time also explains why the error bars decrease with increasing temperature. A detailed discussion on why the addition of uranium and thorium significantly increases the viscosity of the salt is provided in a later section.

3.3 Structural Quantities

3.3.1 Pair Distribution Function

The pair distribution function (PDF) g_{ab} tells us about the distribution of particles of type b around particles of type a. More specifically, it quantifies how much larger the distribution of particle b is around a when compared to its bulk density. Thus, it tell us about the structure of the material. Mathematically,

$$g_{ab}(\mathbf{r}) = \frac{\langle \rho_{ab}(\mathbf{r}) \rangle}{\rho_b}. \tag{3.9}$$

where $\langle \rho_{ab}(\mathbf{r}) \rangle$ is the average particle density of particle b at a distance $\mathbf{r}$ from a particle a, and ρ_b is the bulk density of particle b. Intuitively, Equation 3.9 is simply counting the average number of particles b that fall within a small volume $\mathrm{d}V$ centered around a point in space represented by $\mathbf{r}$ when taking the position of a particle a as the origin. For that reason, a perhaps more clear way to write the PDF is

$$g_{ab}(\mathbf{r}) = \frac{1}{dV\rho_b} \left\langle \frac{1}{N_a} \sum_a \sum_b \delta[\mathbf{r} - (\mathbf{r}_b - \mathbf{r}_a)] \right\rangle \tag{3.10}$$

where the ensemble average $\langle ... \rangle$ is over all frames in the MD simulation since the PDF is a static quantity, and the sum is over all particles a and b in the system. However, we are typically more interested in the radial distribution of one atom around another, ignoring the angular dependence. Hence, the true quantity of interest is a specific case of the pair distribution function, called the radial distribution function (RDF)

$$g_{ab}(r) = \frac{1}{4\pi r^2 dr \rho_b} \left\langle \frac{1}{N_a} \sum_a \sum_b \delta(r - |\mathbf{r}_b - \mathbf{r}_a|) \right\rangle. \tag{3.11}$$

The RDF provides information on the relative density of the particle b with respect to its bulk density within a spherical shell of thickness dr centered around particle a. Numerically, the counting performed by the Kronecker delta $\delta(r - |\mathbf{r}_b - \mathbf{r}_a|)$ for each r turns into a histogram whose bins represent different spherical shells. To calculate the RDF we simply count the number of particles b within each spherical shell and normalize it by the expected number of particles b to lie in that spherical shell according to its bulk density ρ_b (i.e. assuming no structure). For example, $g(r')_{ab} = c$ means that the particle density of b at a distance of r' from a is c times higher than its bulk density ρ_b. Therefore, in a structureless material like a monoatomic ideal gas the RDF is always equal to one beyond the r_{min} denoting the gas particle radius.

Figure 3.6 depicts the radial distribution function of F-F and F-cation for the three simulated systems and their average coordination number over the simulated temperature range. The addition of uranium and thorium, which are multivalent cations, causes significant structural changes in the salt by pulling fluorine atoms towards them. This is quantified by the steep peak on the RDF for F-U and F-Th along with their respective coordination numbers of 7.6 and 8.0. These two features suggest the existence of $[XF_7]^{3-}$, $[XF_7]^{3-}$, $[XF_8]^{4-}$, and $[XF_9]^{5-}$ clusters where X = Th or U. By inspecting the MD simulation using VMD [36], the existence of these clusters were confirmed. $[XF_7]^{3-}$ was the most prevalent one, while $[XF_8]^{4-}$ and $[XF_9]^{5-}$ only existed for short periods of time. These clusters were also observed by Guo *et al.* [37] while studying ThF_4 in unary fluoride salts such as LiF, NaF, and KF. Furthermore, the slightly higher coordination number of the thorium system can be tied to its marginally higher viscosity when compared to the uranium system.

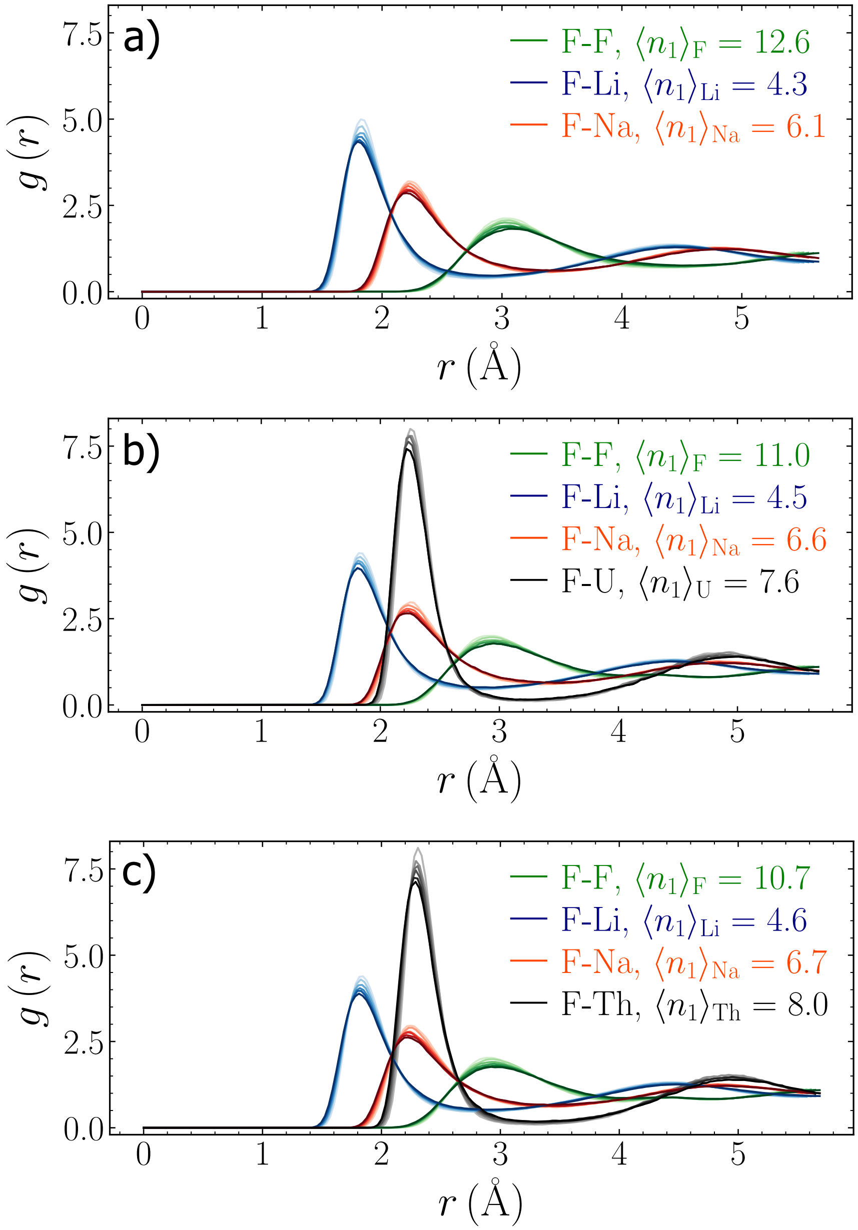

Figure 3.6: Radial distribution function for **a)** pure FLiNa, **b)** FLiNa + UF$_4$, **c)** FLiNa + ThF$_4$. Each color is representing the radial distribution function of F with a different cation, and each curve is representing a different temperature. Among them, the lighter-shaded curves correspond to the lower temperatures.

3.3.2 Structure Factor

The structure factor is related to the pair distribution function by a Fourier transform

$$S(\mathbf{k}) = 1 + \rho \int e^{(-i\mathbf{k}\cdot\mathbf{r})} g(\mathbf{r})\, d\mathbf{r} \tag{3.12}$$

which means that the structure factor carries the same information as the pair distribution function, but this information is encoded in a different domain. However, the structure factor has the advantage that it can be directly obtained from neutron and x-ray scattering experiments. Intuitively, the structure factor is connected to the amplitude spectrum of the plane wave decomposition of the relative particle density distribution. Mathematically, each $S(\mathbf{k}')$ relates to the amplitude of a specific plane wave $\exp(-i\mathbf{k}'\cdot \mathbf{r})$ used in the Fourier transform of the PDF. Thus, the structure factor gives information on the range and degree of spatial correlations between particles. More precisely, $S(\mathbf{k})$ tells the amplitude of spatial correlations or variations along the direction of the wave vector $\hat{\mathbf{k}} = \mathbf{k}/|\mathbf{k}|$ over length scales of $2\pi/|\mathbf{k}|$. Although very useful, the structure factor encodes only amplitude information and misses all phase information (i.e. the relative phase between the plane waves). An alternative way to understand the structure factor is as a two-point correlation function

$$S(\mathbf{k}) = \frac{1}{N} \langle \rho_{\mathbf{k}}\, \rho_{\text{-}\mathbf{k}} \rangle \tag{3.13}$$

where $\rho_{\mathbf{k}}$ is the Fourier transform of the local density $\rho(\mathbf{r})$. Working on Equation 3.13 yields

$$S(\mathbf{k}) = \frac{1}{N} \sum_{i} \sum_{j} \mathrm{e}^{-i\mathbf{k}\cdot(\mathbf{r}_i - \mathbf{r}_j)} \tag{3.14}$$

where both sums are over all atoms in the system. Weighting the $S(\mathbf{k})$ by the proper coherent neutron scattering lengths allow it to be directly compared to neutron diffraction experiments [38]. In the same spirit as the PDF, our goal is often to identify spatial correlations of specific length scales, regardless of its direction. This means that we are concerned only with the magnitude of the plane wave's k-vector, rather than its direction in reciprocal space. The structure factor then becomes

$$S(k) = \frac{1}{N} \sum_i \sum_j \mathrm{e}^{-ik|\mathbf{r}_i - \mathbf{r}_j|} \tag{3.15}$$

where $k = |\mathbf{k}|$ is the wavenumber. Figure 3.7 illustrates the neutron-weighted structure factor for the three systems. Because the simulation box is finite and due to the use of boundary conditions, there is a finite number of allowed k-vectors. Since smaller k-vectors accounts for correlations in longer scales, the smallest k-vector represents the longest spatial correlation detectable in the simulation box, and its magnitude is constrained by the box size according to $k = 2\pi/L$ where L is the length of the cubic box. The small peak at the second smallest k, indicated by an arrow in Figure 3.7, suggests that the addition of thorium and uranium to FLiNaK introduces an intermediate structural ordering. This so-called pre-peak is located at $k = 1.12$ Å^{-1} and corresponds to structures with length scales of 5.6 Å. These structures most likely correspond to the clusters observed in the simulation and discussed in the previous section. In fact, as shown in the snapshots in Figures 3.7b and 3.7c, these clusters tend to aggregate and form longer networks. However, the length scales needed to investigate such networks are not accessible via FPMD. A potential approach to investigate these structures involves utilizing a neural network potential trained on FPMD data. This method was employed by Chahal *et al.* [39] in their study of ZrF_4 networks in FLiNa.

The emergence of intermediate-range ordering in FLiNa when uranium and thorium are added is very important and carries multiple implications. This directly influences thermophysical properties, like viscosity, and alters the dynamics of the liquid. It appears that in general the addition of a multivalent cation species to fluoride salts promotes cluster formation. Chahal *et al.* [39] and Guo *et al.* [37] observed the same structural changes when ZrF_4 is added into LiF-NaF and when ThF_4 is added to unary fluoride salts such as LiF and KF, respectively. These clusters, composed of multivalent cations surrounded by fluorine atoms, seem to aggregate over time and form network structures. As a direct consequence of these extended spatial correlations, the viscosity of the salt increases.

3.4 Dynamic Quantities

To study the diffusion of individual particles dynamic quantities are needed. In statistical mechanics, time-correlation functions such as van Hove correlation and intermediate scattering function are used to do so. Because the main interest lies in understanding the bulk diffusion of thorium and uranium atoms in the molten salt, only the self component of these two time correlation functions are calculated.

3.4.1 Self van Hove Correlation

The self van Hove correlation $G_s(\mathbf{r}, t)$ tells how likely it is to find a particle at position $\mathbf{r}$ at time t given that it was at the origin $\mathbf{r} = 0$ at $t = 0$. Mathematically, it is given by

$$G_s(\mathbf{r}, t) = \left\langle \frac{1}{N} \sum_i \delta[\mathbf{r} - (\mathbf{r}_i(t) - \mathbf{r}_i(0))] \right\rangle \tag{3.16}$$

where the sum is over all particles of interest and $\langle ... \rangle$ denotes an ensemble average over different sets of particle's initial conditions (i.e. over independent simulations with different initial configurations). If the MD simulation is longer than the longest time scale relevant to the study, it is possible to compute the ensemble average over different time windows within that single simulation, with each time window being

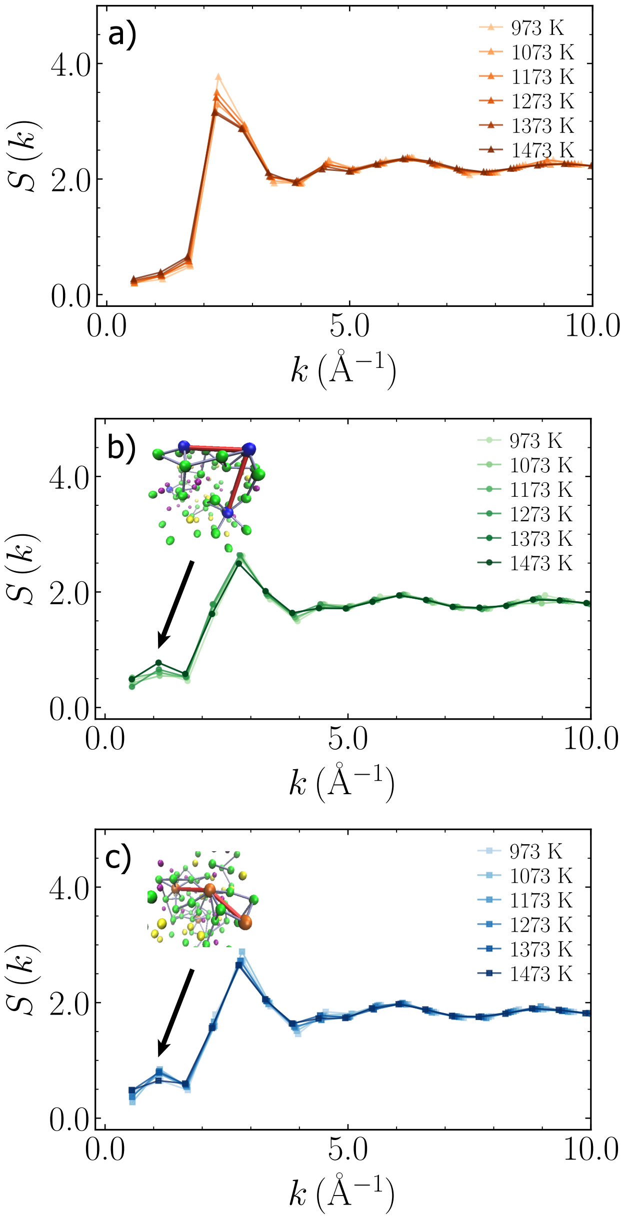

Figure 3.7: Neutron-weighted structure factor for **a)** pure FLiNa, **b)** FLiNa + UF_4, **c)** FLiNa + ThF_4. Each curve is representing a different temperature. Among them, the lighter-shaded curves correspond to the lower temperatures. The pre-peak at $k \approx 1.12\text{Å}^{-1}$ is indicated by an arrow.

as long as the longest time scale of interest. In the flavor described by Equation 3.16, the self van Hove correlation yields the fractional particle occupation at each chunk of space as a function of time. Intuitively, it can be thought as a time-dependent 3-dimensional histogram of particle's displacements. However, in most cases the self van Hove is divided by the volume of that chunk of space (i.e. bin volume) and it reads

$$G_s(\mathbf{r},t) = \frac{1}{dV}\left\langle \frac{1}{N}\sum_i \delta[\mathbf{r} - (\mathbf{r}_i(t) - \mathbf{r}_i(0))] \right\rangle \tag{3.17}$$

where dV is the volume of a tiny portion of space centered around $\mathbf{r}$. In the format of Equation 3.17, the self van Hove becomes a time-dependent volumetric probability density, meaning that integrating it over the entire space yields 1. Note that $G_s(\mathbf{r},t)$ normalized by the volume is precisely the quantity we obtain when solving the diffusion equation. In the same way as the structure factor and the PDF, it is customary to neglect the angular dependency and focus on the net distance travelled by the particle. In this case, the self van Hove correlation becomes

$$G_s(r,t) = \frac{1}{4\pi r^2 dr}\left\langle \frac{1}{N}\sum_i \delta[r - |\mathbf{r}_i(t) - \mathbf{r}_i(0)|] \right\rangle \tag{3.18}$$

The difference is that now $G_s(r,t)$ is a radial probability density, meaning that calculating the integral $\int_{r_1}^{r_2} G_s(r,t')\,4\pi r^2 dr$ for a given time $t = t'$ yields the probability of finding the particle inside a spherical shell centered at the particle's origin and defined by $r = [r_1, r_2]$ at that specific time. Intuitively, we can think of $G_s(r,t)$ as a time-dependent histogram where each bin represents a spherical shell.

Figure 3.8 depicts the self van Hove correlation for uranium and thorium in FLiNa. It shows that the time evolution profile of the radial probability density for uranium and thorium in FLiNa are very similar. Each curve resembles a Gaussian and illustrates the probability density of finding the particle at a distance r from

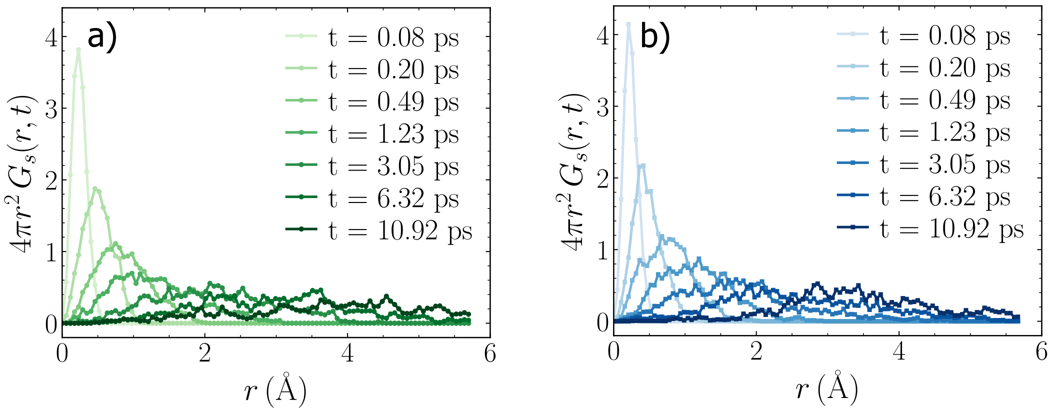

Figure 3.8: Self van Hove correlation for **a)** Uranium **b)** Thorium in FLiNa at the highest simulated temperature 1473 K.

its reference origin after different time intervals. As time progresses, the probability density becomes more spread out. This happens because as the simulation advances in time, the particle gradually decorrelates with its initial state due to collisions with other nearby particles. But since this is a random process, the uncertainty regarding the distance range that the particle can be found from its origin increases with time, and this is what Figure 3.8 is showing.

3.4.2 Self-Intermediate Scattering Function

The self-intermediate scattering function is the Fourier transform of the self van Hove correlation and is generally given by

$$F_s(\mathbf{k},t) = \int e^{-i\mathbf{k}\cdot\mathbf{r}} G_s(\mathbf{r},t)\,d\mathbf{r} \tag{3.19}$$

The self-intermediate scattering function depicts how the amplitudes of the plane waves used in the Fourier decomposition of the self van Hove correlation evolve in time. Since the $F_s(\mathbf{k},t)$ is related to the $G_s(\mathbf{r},t)$, it represents the diffusion of individual particles. Because the particle at $t = 0$ is always at its reference origin, the self van Hove correlation is a delta function in space, and since the self intermediate scattering function is its Fourier transform, it must be equal to one for all **k**'s at $t = 0$. This is intuitive because to achieve infinitely precise spatial resolution and construct a function that is perfectly localized (delta function), the superposition of infinitely many plane waves with different wave vectors is required. Numerically, the self-intermediate scattering function is calculated by

$$F_s(\mathbf{k}, t) = \frac{1}{N} \left\langle \sum_i e^{-i\mathbf{k}\cdot(\mathbf{r}_i(t)-\mathbf{r}_i(0))} \right\rangle \tag{3.20}$$

where the sum is performed over all particles of interest and the ensemble average $\langle ... \rangle$ is over different initial conditions. Because we are often interested in the magnitude of particle displacements and not on its direction, Equation 3.20 simplifies to

$$F_s(k, t) = \frac{1}{N} \left\langle \sum_i e^{-ik|\mathbf{r}_i(t)-\mathbf{r}_i(0)|} \right\rangle \tag{3.21}$$

Figure 3.9 illustrates the self-intermediate scattering function of uranium and thorium in FLiNa. Each curve in the plot depicts a diffusion mode. The relaxation time τ of a mode is defined as the time it takes for the $F_s(k, t)$ to decay to about 36% $(1/e)$ of its initial value. Figure 3.9 shows that as the wavenumber k increases, the corresponding curve decays to zero faster, meaning that the relaxation time decreases. Intuitively, plane waves with large wavenumbers are sensitive to small spatial variations, and in this context they probe diffusion processes that happen over small length scales. Thus, in a spatially smooth function the contribution of these long plane waves would be very small, resulting in tiny amplitudes associated with these modes. Since the $F_s(k, t)$ and the $G_s(r, t)$ are Fourier pairs, the rapid decay in time of the amplitude of modes with high spatial frequency or wavenumber k is related to the smoothing of the radial probability density $4\pi r^2 G_s(r, t)$ with time

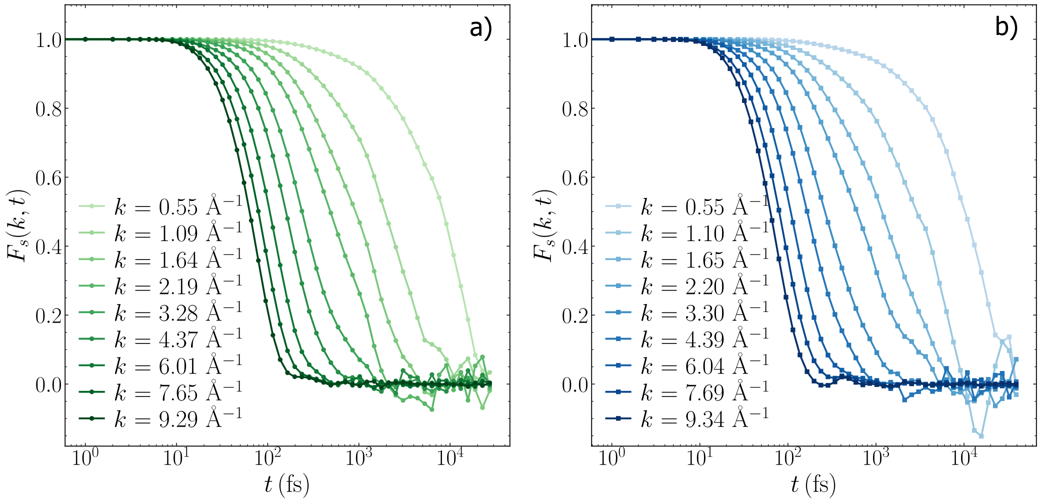

Figure 3.9: Self-intermediate scattering function for **a)** Uranium **b)** Thorium in FLiNa at the highest simulated temperature 1473 K.

shown in Figure 3.17. Therefore, the longer modes dominate at long time scales.

3.4.3 Singwi-Sjölander Jump Diffusion Model

The Singwi-Sjölander (S-S) model of jump diffusion [40] was employed to study the diffusion process. In its simplest form, it models the diffusion process as a series of discrete jumps interspaced by caging periods where the particle is essentially trapped by its first coordination shell. Note that even though this is not the general physical picture of what is happening in liquids, the S-S model is still useful as a comparison tool due to its effectiveness in expressing the diffusion process in terms of two simple variables: the residence time and the jump length. The residence time corresponds to the average time interval between two consecutive jumps. It indicates how strong the particle's caging is, or the effectiveness of nearest neighbors in restraining the particle's diffusion. As for the jump length, it represents the average distance travelled by a particle before it becomes trapped again. The S-S model consists of fitting the inverse relaxation time (extracted from the self-intermediate scattering function) as a function of the wavenumber squared using the following functional form

$$\frac{1}{\tau} = \frac{Dk^2}{1 + Dk^2\tau_0} \tag{3.22}$$

where k is the wavenumber, D the diffusion coefficient, and τ_0 the average residence time. The fitting is shown in Figure 3.10. Except at the lowest temperature, there is a very good agreement between the S-S model and the simulation results. The lesser agreement at the lowest temperature is probably due to the closer proximity to the salt's melting point. The residence time is readily available from the fit since it is just a fitting parameter, while the mean squared jump length can be calculated using the following relation

$$\langle l^2 \rangle = 6D\tau_0 \tag{3.23}$$

The diffusion coefficient for uranium and thorium in FLiNa can be found from Figure 3.10 by doing a linear fit using the smallest k's (hydrodynamic limit) and extracting the slope of this line. Here, only the four smallest wavenumbers were used. The reason why only the smallest k's are considered is because they are representing diffusion over larger length scales, which is our primary interest. The plane waves with a large wave number represent diffusion processes over small length scales that are noisy and not representative of the long-time diffusion behavior of the particle.

Figure 3.11 shows the average residence time, mean squared jump length and diffusion coefficient for both thorium and uranium in FLiNa. Because the diffusion coefficient increases with temperature, there is a corresponding increase of the jump length and decrease of the residence time with temperature. Figures 3.11a and 3.11b reveals that while the average jump length of uranium is longer than thorium, its residence time is higher. This two factors offset each other and yield very similar diffusion coefficients as shown in Figure 3.11c. The slightly higher diffusion coefficient

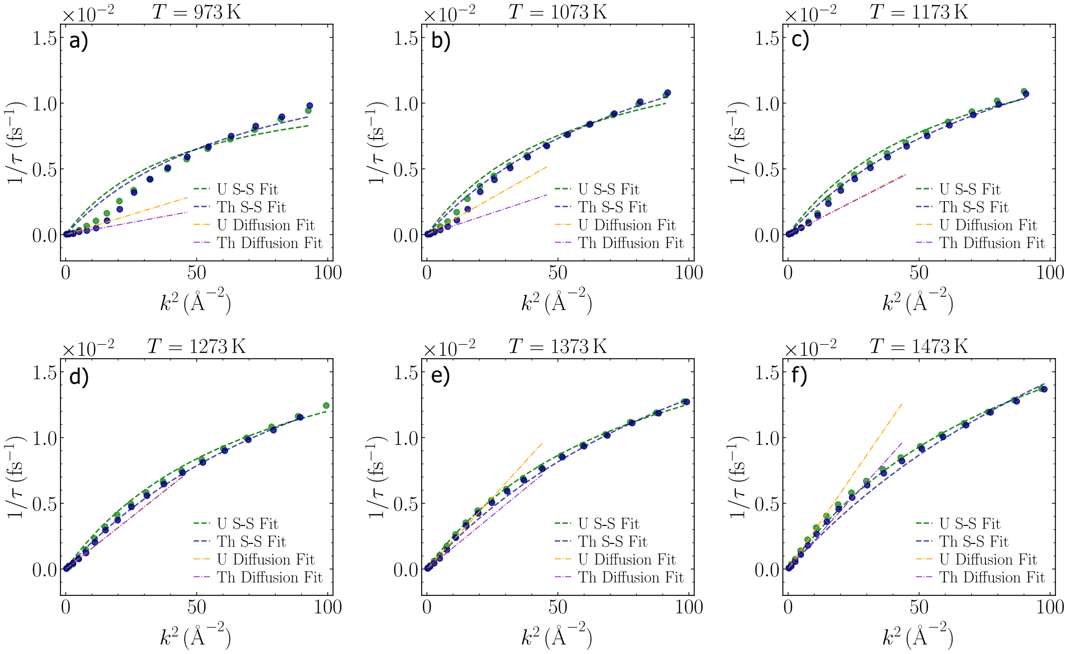

Figure 3.10: Inverse relaxation time versus the wavenumber squared at different temperatures **a)** 973 K; **b)** 1073 K; **c)** 1173 K; **f)** 1273 K; **e)** 1373 K; **f)** 1473 K; for FLiNa + UF$_4$ and FLiNa + ThF$_4$. The green and blue dashed lines correspond to the S-S fitting on the data points extracted from the self-intermediate scattering function of uranium and thorium respectively. The linear fits for uranium (yellow) and thorium (purple) considered only the four lowest k values. The slope of this linear fit is the diffusion coefficient at that specific temperature.

of uranium can be connected to its smaller viscosity and coordination number. The activation energies for uranium and thorium are also very similar, with values of 0.40 eV and 0.39 eV respectively. The close diffusion coefficients for uranium and thorium are consistent with literature results, which suggests that the diffusion coefficients of lanthanides and actinides ions in molten salts depend mostly on their valence, and show almost no dependence on their crystallographic radii [41].

3.5 The Link Between Viscosity and Structure

In liquids, intermediate-range ordering refers to an organized arrangement of atoms or molecules over distances ranging from 5-20 Å according to Elliot's [42] definition.

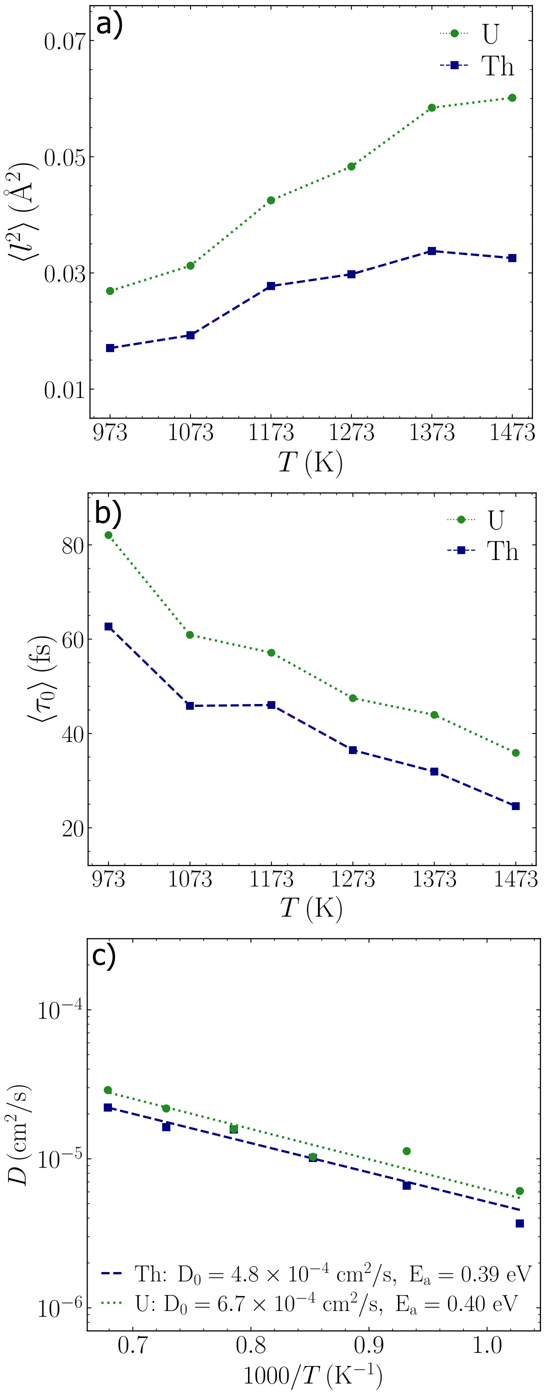

Figure 3.11: **a)** Average jump length as a function of temperature for uranium (green) and thorium (blue) in FLiNa. **b)** Average residence time as a function of temperature. **c)** Diffusion coefficient for uranium and thorium as a function of temperature.

These structures are nearly ubiquitous and encountered in a wide range of liquid systems, such as ionic liquids, metallic melts, and protein solutions [43]–[47]. Their hallmark is the appearance of a pre-peak in the structure factor [48]–[50], which indicates spatial correlations beyond the length scales represented by the main structure factor peak. Although intermediate-range ordering appears to impact the thermophysical and transport properties of the liquid [39], [41], [51], a clear connection or underlying mechanism has not been identified yet. For specific systems such as polymer, there is a general connection between structure and viscosity. Particularly, the structure and weight of the polymer chain is known to influence viscosity [52], [53]. In molten salts, however, there isn't any theory connecting structural features to viscosity. In this section, this link for molten salts is discussed and a mechanism that can explain the relation between intermediate-range ordering and viscosity is proposed.

The big increase in the salt's viscosity when uranium and thorium are introduced into the pure salt indicates that something new is happening at the atomic level. When uranium and thorium are added into the salt, a pre-peak appears in the structure factor (see Figure 3.7), which is indicative of a intermediate-range ordering that is absent in the pure salt. These extended structures or clusters interact with each other and affect particle interactions, leading to additional fluid flow resistance and therefore viscosity. In the atomic picture, viscosity is related to the degree of correlation between atomic-level stresses [54], [55]. The amount of correlation is then influenced by particle interactions [56], the local atomic environment, and the overall structure of the system.

To further investigate this issue, a closer look into the Green-Kubo relation is needed. As already discussed, this relation describes the macroscopic viscosity in terms of the autocorrelation of the shear components of the macroscopic stress tensor. However, we can further breakdown the macroscopic stress $\sigma^{\alpha\beta}$ into a sum of individual atomic-level contributions:

$$\sigma^{\alpha\beta} = \sum_i \sigma_i^{\alpha\beta} \tag{3.24}$$

where $\sigma_i^{\alpha\beta}$ is the atomic-level stress tensor and the sum is over all atoms in the system. The atomic-level stress is formally defined as the first order local response in energy to a homogeneous strain [57]. Intuitively, the atomic stress arises from a mismatch between the size of the atom and the size and shape of its atomic site, i.e. the volume of space in the system dedicated to it. If the designated atomic site is larger than the actual atom size, a tensile stress develops. Conversely, if the atomic site is smaller than the atom size, a compressive stress appears. The atomic stress experienced by an atom is related to the spatial distribution of its neighbors, as this determines the size and shape of the atomic site. The neighbor distribution, on the other hand, depends on the interactions between atoms, so the atomic-level stress ultimately depends on the potential energy surface. The Green-Kubo relation for viscosity can then be rewritten in terms of the atomic-level stresses as

$$\eta = \lim_{\tau' \to \infty} \frac{V}{k_b T} \int_0^{\tau'} \left\langle \sum_i \sigma_i^{\alpha\beta}(t_0 + \tau) \cdot \sum_i \sigma_i^{\alpha\beta}(t_0) \right\rangle \, d\tau \tag{3.25}$$

and the autocorrelation can be further expanded as

$$\begin{aligned} \left\langle \sum_i \sigma_i^{\alpha\beta}(t_0 + \tau) \cdot \sum_i \sigma_i^{\alpha\beta}(t_0) \right\rangle = & \sum_i \langle \sigma_i^{\alpha\beta}(t_0 + \tau) \ \sigma_i^{\alpha\beta}(t_0) \rangle \\ & + \frac{1}{2} \sum_i \sum_{j \neq i} \langle \sigma_i^{\alpha\beta}(t_0 + \tau) \ \sigma_j^{\alpha\beta}(t_0) \rangle \end{aligned} \tag{3.26}$$

for $i = j = [1, N]$ where N is the total number of atoms in the system. This expansion is particularly informative because it breaks down the macroscopic stress autocorrelation into atomic-level stress autocorrelations and cross-correlations. The first term on the right-hand side represents the correlation of the atomic stress of an atom i with itself, while the second term refers to the correlation between the atomic stress of atom i and all other atoms j in the system. Thus, Equations 3.25 and 3.26 put together directly connect the macroscopic viscosity to atomic-level quantities. This link helps elucidate the role that intermediate-range structures play in the macroscopic viscosity. Two atoms that are part of the same intermediate-range structure (e.g. a cluster) are more correlated than two arbitrary atoms in the bulk liquid. This means that the amplitudes of the atomic stress cross-correlations between atoms within the same cluster are generally higher than the amplitudes of the cross-correlations between atoms that are not. Atoms that are part of the same cluster have stronger interactions tying them together, so it is reasonable to assume that the properties of these atoms will exhibit a higher degree of correlation when compared to bulk atoms. On top of that, because the atoms in these structures are more restrained, it also takes longer for the atomic shear stress autocorrelations to decay. As a direct consequence of these increased correlations of the atoms in the cluster, the viscosity as described by Equations 3.25 and 3.26 increases.

An alternative explanation is in terms of shear waves. Although liquids generally don't support the propagation of shear waves at macroscopic length scales, they do support them at the atomic scale over lengths of tenths of Angstroms [54]. These waves die-off very quickly because liquids lack the necessary rigidity to support the transverse motion with respect to the direction of wave propagation. However, because intermediate-range structures locally resemble amorphous solids (if we zoom into these structures and ignore the background we cannot tell whether it is a piece of an amorphous solid or an intermediate-range structure in a liquid), they can better sustain shear waves when compared to the bulk liquid. Therefore, the presence of intermediate-range structures extends the range of propagation of shear waves, causing them to take longer to be suppressed and disappear. Because shear waves are the mechanism by which the atomic stress of two atoms in the system correlates or “connects“, this extended propagation range leads to a greater atomic shear stress cross-correlation and therefore to a higher viscosity. Mathematically, the second term in the right-handed side of Equation 3.26 takes longer to decay to zero.

Chapter 4

Conclusion & Future Work

4.1 Conclusion

This work connects the structure of the liquid to its thermophysical and dynamic properties and therefore highlights the importance of understanding the salt's structure. It shows how the properties of molten salts can evolve in an unexpected and non-linear fashion over time, which has important implications in the field of MSRs. As time evolves and fuel is burned, multivalent cation species appear in the molten salt and form intermediate-range structures. As a consequence, the amplitude of the atomic-level shear stresses correlations of atoms in these structure increases, and this leads to an increases in the viscosity by a significant amount. For the examples shown here, having only 9.1% mol of ThF_4 or UF_4 in pure FLiNa is enough to increase viscosity by 20-30%. Because viscosity is an important part of any multiphysics simulation of a MSR, it is important to consider its evolution over time to obtain accurate simulation results. Moreover, the big increase in the viscosity contrasts with other thermophysical properties, such as molar specific heat and thermal expansion, that doesn't seem to be affected much by the addition of fuel elements and subsequent formation of intermediate-range ordering structures.

4.2 Future Work

One promising venue to extend this work is to use machine-learned interatomic potentials. It comprises of training a neural network using DFT data with the goal of learning the forces exerted on each atom given its atomic environment. However, to successfully train a neural network potential, several DFT simulations spanning different pressures, temperatures, and system compositions must be performed. Thus, on top of the already expensive network training, the dataset creation can also be very costly. Additionally, the system can become trapped in a local free energy minimum for most of the trajectory, resulting in a dataset comprised mostly of very similar configurations, which negatively impacts the training of the neural network. Therefore, efficient ways of sampling different configurations and creating a diverse and reliable dataset must be sought.

An interesting approach to automate the creation of such datasets was proposed by Justin Smith *et al.* in [58]. It involves initially training an ensemble of neural network potentials using a dataset derived from single-point DFT calculations on randomly initialized configurations. MD simulations driven by this neural network ensemble are then performed. If there is a discrepancy among the ensemble members regarding the energies and/or forces in a specific frame, the contentious configuration is flagged and a single-point DFT calculation is performed on it. Such disagreement is quantified by the standard deviation of the energies and forces; if the standard deviation exceeds a predetermined threshold, then the frame is flagged. This whole process is repeated until no more configurations are flagged, and at that point we are left with a diverse and robust dataset.

Once a robust dataset has been constructed, the production training can start. There are several neural network potential packages available, including Nequip

[59], HIPPYNN [60], DeepMD [61], and TorchMD-Net [62] to name a few. The most recent neural network potentials such as Nequip use equivariant graph neural networks that respect the translational, permutational, rotational symmetries of the potential energy surface. Once the training finishes, machine learning driven molecular dynamics simulations are performed to probe length and time scales that were previously inaccessible. By conducting large-scale MD simulations using machine-learned interatomic potentials, it is now possible to calculate properties such as thermal conductivity and melting point, which are challenging to compute using FPMD. These properties require large simulation boxes and long trajectories for accurate calculation that are often beyond the capabilities of FPMD. Thermal conductivity can be calculated through its own G-K relation, in a similar fashion to viscosity. The only difference is that instead of integrating the autocorrelation of the shear stress, for thermal conductivity we integrate the autocorrelation of the heat current. However, the time required for the autocorrelation of the heat current to decay to zero can span hundreds of picoseconds, in contrast to the few picoseconds typically needed in molten salts for the autocorrelation of the shear stress to decay. For that reason, it is not possible to perform reliable calculations of thermal conductivity using FPMD.

As for the melting point, which is one of the most difficult properties to calculate using FPMD, there are several different methods available for its calculation using classical MD. These methods are either free energy-based, or direct methods, and most of the direct methods are interface-based methods. The most straightforward method is to simulate a system that contains both liquid and solid phases in equilibrium at different temperatures, and find the temperature where both phases coexist (i.e. there is no change in the proportion of solid to liquid over time) [63]. Yong Zhang *et al.* compared numerous different methods of calculating melting point from MD simulations in their literature review [64].

Ultimately, conducting large-scale MD simulations driven by machine-learned potentials leverages GPU computing, offering a significant advantage as most of DFT codes are CPU-bound. This approach facilitates even larger simulations, potentially involving millions of atoms, while maintaining first-principles accuracy.

Another natural extension of this work is to attempt to prove the newly proposed ideas. Specifically, this involves showing the relationship between intermediate-range order and viscosity in general liquids, and the hypothesis that the addition of multivalent cations to fluorine or chlorine salts results in the formation of intermediate-range ordering structures.

The investigation of the connection between intermediate-range ordering and viscosity can be conducted through large scale MD, either driven by classical force fields or neural network potentials. Under this setting, the atomic stress tensor of each atom can be computed, a feat that is not possible using FPMD. Then, the atomic-level shear stress cross-correlation between atoms that are part of the same intermediate-range structures can be computed and compared to the stress correlation between atoms in the bulk liquid. If the amplitude of the cross-correlation between the two atoms in the cluster is generally greater than the two atoms in the bulk at equivalent distances, then this would prove the proposed link between intermediate-range structures and viscosity. Furthermore, this idea leads us to expect that the autocorrelation of the atomic shear stress for an atom that are part of an intermediate-range structure will take longer to decay to zero when compared to a bulk atom. This can also be readily evaluated given that the atomic-level stresses were calculated.

Finally, large-scale MD simulations can be utilized to analyze the formation of intermediate-range structures and network complexes in fluoride and chloride salts upon the addition of multivalent cations. Simulations can encompass various salts with distinct compositions and temperatures, as well as cations of different sizes and valences. If the proposed idea is correct, then the formation and prevalence of these structures and networks will depend primarily on the valance and concentration of the multivalent cation. Although evaluating this idea is straightforward, it necessitates performing several simulations.

References

[1] M. Rosenthal, P. Kasten, and R. Briggs, “Molten-salt reactors—history, status, and potential,” *Nuclear Applications and Technology*, vol. 8, no. 2, pp. 107–117, 1970.

[2] M. Kelly, “Removal of rare-earth fission products from molten-salt reactor fuels by distillation,” *Transactions of the American Nuclear Society (US)*, vol. 8, 1965.

[3] D. LeBlanc, “Molten salt reactors: A new beginning for an old idea,” *Nuclear Engineering and design*, vol. 240, no. 6, pp. 1644–1656, 2010.

[4] C. W. Forsberg, “Molten-salt-reactor technology gaps,” in *Proc. 2006 International Congress on Advances in Nuclear Power Plants (ICAPP’06)*, Citeseer, 2006, pp. 4–8.

[5] B. Mignacca and G. Locatelli, “Economics and finance of molten salt reactors,” *Progress in Nuclear Energy*, vol. 129, p. 103 503, 2020.

[6] J. Serp, M. Allibert, O. Beneš, *et al.*, “The molten salt reactor (msr) in generation iv: Overview and perspectives,” *Progress in Nuclear Energy*, vol. 77, pp. 308–319, 2014.

[7] G. Zheng, H. Wu, J. Wang, S. Chen, and Y. Zhang, “Thorium-based molten salt smr as the nuclear technology pathway from a market-oriented perspective,” *Annals of Nuclear Energy*, vol. 116, pp. 177–186, 2018.

[8] A. Ho, M. Memmott, J. Hedengren, and K. M. Powell, “Exploring the benefits of molten salt reactors: An analysis of flexibility and safety features using dynamic simulation,” *Digital Chemical Engineering*, vol. 7, p. 100 091, 2023.

[9] B. M. Elsheikh, “Safety assessment of molten salt reactors in comparison with light water reactors,” *journal of radiation research and applied sciences*, vol. 6, no. 2, pp. 63–70, 2013.

[10] B. M. Chisholm, S. L. Krahn, and A. G. Sowder, “A unique molten salt reactor feature–the freeze valve system: Design, operating experience, and reliability,” *Nuclear Engineering and Design*, vol. 368, p. 110 803, 2020.

[11] K. Sridharan and T. Allen, “12 - corrosion in molten salts,” in *Molten Salts Chemistry*, Oxford: Elsevier, 2013, pp. 241–267.

[12] B. D’Souza, W. Zhuo, Q. Yang, A. Leong, and J. Zhang, “Impurity driven corrosion behavior of haynes® 230® alloy in molten chloride salt,” *Corrosion Science*, vol. 187, p. 109 483, 2021.

[13] S. Delpech, C. Cabet, C. Slim, and G. S. Picard, “Molten fluorides for nuclear applications,” *Materials Today*, vol. 13, no. 12, pp. 34–41, 2010.

[14] T. R. Nelson, A. J. White, J. A. Bjorgaard, *et al.*, “Non-adiabatic excited-state molecular dynamics: Theory and applications for modeling photophysics in extended molecular materials,” *Chemical reviews*, vol. 120, no. 4, pp. 2215–2287, 2020.

[15] R. J. Bartlett and M. Musiał, “Coupled-cluster theory in quantum chemistry,” *Reviews of Modern Physics*, vol. 79, no. 1, p. 291, 2007.

[16] C. Møller and M. S. Plesset, “Note on an approximation treatment for many-electron systems,” *Physical review*, vol. 46, no. 7, p. 618, 1934.

[17] P. Hohenberg and W. Kohn, “Inhomogeneous electron gas,” *Physical review*, vol. 136, no. 3B, B864, 1964.

[18] J. P. Perdew, K. Burke, and M. Ernzerhof, “Generalized gradient approximation made simple,” *Physical review letters*, vol. 77, no. 18, p. 3865, 1996.

[19] J. P. Perdew, K. Burke, and Y. Wang, “Generalized gradient approximation for the exchange-correlation hole of a many-electron system,” *Physical review B*, vol. 54, no. 23, p. 16 533, 1996.

[20] W. Kohn and L. J. Sham, “Self-consistent equations including exchange and correlation effects,” *Physical review*, vol. 140, no. 4A, A1133, 1965.

[21] G. Kresse and D. Joubert, “From ultrasoft pseudopotentials to the projector augmented-wave method,” *Physical Review B*, vol. 59, 3 1999.

[22] G. Kresse and J. Furthmü, "Efficient iterative schemes for ab initio total-energy calculations using a plane-wave basis set," *Physical Review B*, vol. 54, 16 1996.

[23] J. P. Perdew, K. Burke, and M. Ernzerhof, "Generalized gradient approximation made simple," *Physical Review Letters*, vol. 77, 18 Oct. 1996.

[24] P. E. Blöchl, "Projector augmented-wave method," *Physical review B*, vol. 50, no. 24, p. 17 953, 1994.

[25] S. Grimme, J. Antony, S. Ehrlich, and H. Krieg, "A consistent and accurate ab initio parametrization of density functional dispersion correction (dft-d) for the 94 elements h-pu," *The Journal of chemical physics*, vol. 132, no. 15, 2010.

[26] S. L. Dudarev, G. A. Botton, S. Y. Savrasov, C. Humphreys, and A. P. Sutton, "Electron-energy-loss spectra and the structural stability of nickel oxide: An lsda+ u study," *Physical Review B*, vol. 57, no. 3, p. 1505, 1998.

[27] G. Beridze and P. M. Kowalski, "Benchmarking the dft+ u method for thermochemical calculations of uranium molecular compounds and solids," *The Journal of Physical Chemistry A*, vol. 118, no. 50, pp. 11 797–11 810, 2014.

[28] R. Abdullaev, R. Khairulin, and S. Stankus, "Density and thermal expansion of liquid salts lif and lif–naf," *Thermophysics and Aeromechanics*, vol. 30, no. 1, pp. 133–136, 2023.

[29] J. Klimeš, D. R. Bowler, and A. Michaelides, "Chemical accuracy for the van der waals density functional," *Journal of Physics: Condensed Matter*, vol. 22, no. 2, p. 022 201, 2009.

[30] D. Frenkel and B. Smit, *Understanding molecular simulation: from algorithms to applications.* Elsevier, 2023.

[31] W. Zhang and C. He, "Melting of cu nanowires: A study using molecular dynamics simulation," *The Journal of Physical Chemistry C*, vol. 114, no. 19, pp. 8717–8720, 2010.

[32] A. J. McGaughey and M. Kaviany, "Quantitative validation of the boltzmann transport equation phonon thermal conductivity model under the single-mode relaxation time approximation," *Physical Review B*, vol. 69, no. 9, p. 094 303, 2004.

[33] D. A. McQuarrie, *Statistical Mechanics* (Harper's chemistry series). New York: Harper Collins, 1976.

[34] R. Kubo, "The fluctuation-dissipation theorem," *Reports on progress in physics*, vol. 29, no. 1, p. 255, 1966.

[35] A. E. Mattsson and J. M. Wills, "Density functional theory for d-and f-electron materials and compounds," *International Journal of Quantum Chemistry*, vol. 116, no. 11, pp. 834–846, 2016.

[36] W. Humphrey, A. Dalke, and K. Schulten, "Vmd: Visual molecular dynamics," *Journal of molecular graphics*, vol. 14, no. 1, pp. 33–38, 1996.

[37] X. Guo, H. Qian, J. Dai, *et al.*, "Theoretical evaluation of microscopic structural and macroscopic thermo-physical properties of molten af-thf4 systems (a+= li+, na+ and k+)," *Journal of Molecular Liquids*, vol. 277, pp. 409–417, 2019.

[38] N. P. Walter, A. Jaiswal, Z. Cai, and Y. Zhang, "Liquidlib: A comprehensive toolbox for analyzing classical and ab initio molecular dynamics simulations of liquids and liquid-like matter with applications to neutron scattering experiments," *Computer Physics Communications*, vol. 228, pp. 209–218, 2018.

[39] R. Chahal, S. Roy, M. Brehm, S. Banerjee, V. Bryantsev, and S. T. Lam, "Transferable deep learning potential reveals intermediate-range ordering effects in lif–naf–zrf4 molten salt," *JACS Au*, vol. 2, no. 12, pp. 2693–2702, 2022.

[40] K. Singwi and A. Sjölander, "Diffusive motions in water and cold neutron scattering," *Physical Review*, vol. 119, no. 3, p. 863, 1960.

[41] R. Brookes, A. Davies, G. Ketwaroo, and P. A. Madden, "Diffusion coefficients in ionic liquids: Relationship to the viscosity," *The Journal of Physical Chemistry B*, vol. 109, no. 14, pp. 6485–6490, 2005.

[42] S. R. Elliott, "Medium-range structural order in covalent amorphous solids," *Nature*, vol. 354, no. 6353, pp. 445–452, 1991.

[43] W. Hoyer and R. Jödicke, "Short-range and medium-range order in liquid au-ge alloys," *Journal of non-crystalline solids*, vol. 192, pp. 102–105, 1995.

[44] B. Xiufang, S. Minhua, X. Xianying, and Q. Xubuo, "Medium-range order and viscosity of molten cu–23% sn alloy," *Materials Letters*, vol. 57, no. 13-14, pp. 2001–2006, 2003.

[45] P. Luo, Y. Zhai, J. B. Leao, M. Kofu, K. Nakajima, and A. Faraone, “Neutron spin–echo studies of the structural relaxation of network liquid zncl2 at the structure factor primary peak and prepeak,” *The Journal of Physical Chemistry Letters*, vol. 12, no. 1, pp. 392–398, 2020.

[46] L. J. Siqueira and M. C. Ribeiro, “Charge ordering and intermediate range order in ammonium ionic liquids,” *The Journal of chemical physics*, vol. 135, no. 20, 2011.

[47] Y. Liu, L. Porcar, J. Chen, *et al.*, “Lysozyme protein solution with an intermediate range order structure,” *The Journal of Physical Chemistry B*, vol. 115, no. 22, pp. 7238–7247, 2011.

[48] J. Swenson, A. Matic, A. Brodin, L. Börjesson, and W. Howells, “Structure of mixed alkali phosphate glasses by neutron diffraction and raman spectroscopy,” *Physical Review B*, vol. 58, no. 17, p. 11 331, 1998.

[49] A. Ghoufi, “Molecular origin of the prepeak in the structure factor of alcohols,” *The Journal of Physical Chemistry B*, vol. 124, no. 50, pp. 11 501–11 509, 2020.

[50] M. Descamps, V. Legrand, Y. Guinet, A. Amazzal, C. Alba, and J. Dore, ““pre-peak” in the structure factor of simple molecular glass formers,” *Progress of Theoretical Physics Supplement*, vol. 126, pp. 207–212, 1997.

[51] M. Salanne, C. Simon, H. Groult, F. Lantelme, T. Goto, and A. Barhoun, “Transport in molten lif–naf–zrf4 mixtures: A combined computational and experimental approach,” *Journal of Fluorine Chemistry*, vol. 130, no. 1, pp. 61–66, 2009.

[52] P. Debye, “The intrinsic viscosity of polymer solutions,” *The Journal of Chemical Physics*, vol. 14, no. 10, pp. 636–639, 1946.

[53] A. Agasty, A. Wisniewska, T. Kalwarczyk, K. Koynov, and R. Holyst, “Macroscopic viscosity of polymer solutions from the nanoscale analysis,” *ACS Applied Polymer Materials*, vol. 3, no. 5, pp. 2813–2822, 2021.

[54] V. A. Levashov, J. R. Morris, and T. Egami, “Viscosity, shear waves, and atomic-level stress-stress correlations,” *Physical review letters*, vol. 106, no. 11, p. 115 703, 2011.

[55] V. A. Levashov, J. Morris, and T. Egami, “The origin of viscosity as seen through atomic level stress correlation function,” *The Journal of Chemical Physics*, vol. 138, no. 4, 2013.

[56] M. Aniya and M. Ikeda, "The bond strength–coordination number fluctuation model of viscosity: Concept and applications," *Journal of Polymer Research*, vol. 27, pp. 1–8, 2020.

[57] T. Egami, "Atomic level stresses," *Progress in Materials Science*, vol. 56, no. 6, pp. 637–653, 2011.

[58] J. S. Smith, B. Nebgen, N. Mathew, *et al.*, "Automated discovery of a robust interatomic potential for aluminum," *Nature communications*, vol. 12, no. 1, p. 1257, 2021.

[59] S. Batzner, A. Musaelian, L. Sun, *et al.*, "E (3)-equivariant graph neural networks for data-efficient and accurate interatomic potentials," *Nature communications*, vol. 13, no. 1, p. 2453, 2022.

[60] N. Lubbers, J. S. Smith, and K. Barros, "Hierarchical modeling of molecular energies using a deep neural network," *The Journal of chemical physics*, vol. 148, no. 24, 2018.

[61] H. Wang, L. Zhang, J. Han, and E. Weinan, "Deepmd-kit: A deep learning package for many-body potential energy representation and molecular dynamics," *Computer Physics Communications*, vol. 228, pp. 178–184, 2018.

[62] P. Thölke and G. De Fabritiis, "Torchmd-net: Equivariant transformers for neural network based molecular potentials," *arXiv preprint arXiv:2202.02541*, 2022.

[63] Y. Liu, W. Lai, T. Yu, Y. Ma, W. Guo, and Z. Ge, "Melting point prediction of energetic materials via continuous heating simulation on solid-to-liquid phase transition," *ACS Omega*, vol. 4, no. 2, pp. 4320–4324, 2019.

[64] Y. Zhang and E. J. Maginn, "A comparison of methods for melting point calculation using molecular dynamics simulations," *The Journal of chemical physics*, vol. 136, no. 14, 2012.